JOURNAL OF MATERIALS SCIENCE: MATERIALS IN MEDICINE **16** (2005) 947–959

Effect of mineral content on the nanoindentation properties and nanoscale deformation mechanisms of bovine tibial cortical bone

KUANGSHIN TAI[1], HANG J. QI[2,*], CHRISTINE ORTIZ[1]
[1]*Department of Materials Science and Engineering,*
[2]*Department of Mechanical Engineering, Massachusetts Institute of Technology, 77 Massachusetts Avenue, Cambridge, MA 02139, USA*

In this paper, a multitechnique experimental and numerical modeling methodology was used to show that mineral content had a significant effect on both nanomechanical properties and ultrastructural deformation mechanisms of samples derived from adult bovine tibial bone. Partial and complete demineralization was carried out using phosphoric and ethylenediamine tetraacetic acid treatments to produce samples with mineral contents that varied between 37 and 0 weight percent (wt%). The undemineralized samples were found to have a mineral content of ∼58 wt%. Nanoindentation experiments (maximum loads ∼1000 μN and indentation depths ∼500 nm) perpendicular to the osteonal axis for the ∼58 wt% samples were found to have an estimated elastic modulus of ∼7–12 GPa, which was 4–6× greater than that obtained for the ∼0 wt% samples. The yield strength of the ∼58 wt% samples was found to be ∼0.24 GPa; 3.4× greater than that of the ∼0 wt% sample. These results are discussed in the context of *in situ* and *post-mortem* atomic force microscopy imaging studies which show clear residual deformation after indentation for all samples studied. The partially demineralized samples underwent collagen fibril deformation and kinking without loss of the characteristic banding structure at low maximum loads (∼300 μN). At higher maximum loads (∼700 μN) mechanical denaturation of collagen fibrils was observed within the indent region, as well as disruption of interfibril interfaces and slicing through the thickness of individual fibrils leading to microcracks along the tip apex lines and outside the indent regions. A finite element elastic-plastic continuum mechanical model was able to predict the nanomechanical behavior of all samples on loading and unloading.

1. Introduction

Cortical or compact bone is a load-bearing hard tissue that is a well-studied complex biocomposite composed of organic and inorganic material hierarchically organized from the nanometer (nm) up to the macroscopic scale [1]. The fine details of the nano- to microscale structural organization, heterogeneity, geometry, composition, and mechanical properties are known to have a profound effect on the macroscopic mechanical function and dysfunction of the tissue [2–8]. Recently, powerful new high resolution nanotechnological methods have become available and are just starting to be employed in the study of bone at these smaller length scales such as; atomic force microscopy (AFM) imaging [9–12] and nanoindentation [3, 8, 13–18]. In this paper, these techniques are used in combination with other multiple standard characterization methods to investigate a few specific scientific areas of interest using a model system of adult bovine tibial cortical bone.

The first objective of this research was the identification and/or elimination of the many previously suggested nanoscale mechanisms of deformation and the investigation of how these mechanisms are related to elastic, viscoelastic, and plastic nanomechanical properties (e.g. elastic moduli, yield stress, viscoelastic relaxation, etc.). Proposed damage mechanisms in cortical bone include; debonding of mineral-organic interfaces, collagen fibril shear, crosslink scission, denaturation and failure of collagen fibrils, crack formation and propagation, mineral displacement, deformation and structural phase transformation, viscous stretching of the organic component, and rupture of self-healing sacrificial bonds [13, 21–25]. The second aim was to examine the effect of mineral content on ultrastructural deformation mechanisms and to establish its relation to nanomechanical properties. Mineral content is a critical parameter affecting macroscopic mechanical properties [19] that varies with disease (e.g.

**Present address*: Department of Mechanical Engineering, University of Colorado, Boulder, Colorado 80309.

osteoporosis, changes in subchondral trabecular bone with osteoarthritis), prosthetic implantation, weightlessness, ethnicity, and age [20]. Macroscopic tensile experiments performed on cortical bone have shown that increasing calcium content results in an approximately linear increase in stiffness and yield stress, a linear decrease in post-yield stress, work, ultimate strain, and strain-to-failure, and has a minimal effect on ultimate stress [19]. While the origin of the elasticity dependence on mineral content is intuitive from consideration of a standard rule of mixtures approximation for a composite [21, 22], the nanoscale mechanisms by which mineral content affect viscoelastic and plastic behavior are expected to be more complex and are largely unknown at this time. The third and final goal of this study was to assess the ability of two continuum models to capture the nanomechanical behavior of bone and predict its nanoscale materials properties; the first being a purely elastic contact mechanical model [23] and the second consisting of elastic-perfectly plastic finite element analysis (FEA) simulations.

To achieve these objectives, samples of varied mineral content were studied (0–58 wt%), including; undemineralized longitudinal sections of adult bovine tibial cortical bone (cut parallel and tested nanomechanically with the loading direction perpendicular to the long bone axis and the osteonal/Haversian canal axis), and this same type of sample treated with acid to remove various amounts of the mineral component. Characterization of these samples was performed by Raman spectroscopy to measure the chemical composition and mineral-to-organic ratio, back-scattered electron (BSE) imaging to quantify mineral content, standard and environmental scanning electron microscopy (SEM, ESEM) to assess morphology, and AFM to image nanoscale surface topography down to the resolution of individual collagen fibrils. The technique of nanoindentation (controlled compression of a stiff probe tip into a softer specimen of interest while recording the load versus displacement behavior) was employed on these samples at forces ∼100–1000 μN and depths ∼50–500 nm corresponding to a maximum contact area at the maximum load of ∼4.7 μm^2 which contains ∼30 collagen fibrils laterally and ∼3 collagen fibrils vertically. These experiments were combined with *in situ* and *post-mortem* high resolution AFM imaging of the indented area to obtain information on the micro- to nanoscale deformation mechanisms, again down to the level of individual collagen fibrils. Two theoretical models were fit to the nanoindentation data to estimate material properties: (1) the Oliver-Pharr (O-P) method [23] where the initial unloading curve was compared to continuum mechanical theory for an isotropic, elastic half-space with the elastic modulus, E, being the only fitting parameter and (2) elastic-perfectly plastic FEA simulations where the entire loading and unloading curves were fit using two parameters, the elastic modulus and yield stress, σ_y.

It should be noted that since the necessary sample preparation steps do not produce a model system exactly equivalent to that of native bone, a direct quantitative correlation with the mechanical properties of *in vivo* bone tissue is not valid without further theoretical developments. However, trends in nanomechanical properties with various structural parameters, such as mineral content, do provide interesting relevent, and new scientific information. In addition, the samples studied here are in closer-to-physiological conditions than typically reported (e.g. no alcohol dehydration, embedding, chemical fixation, etc.) and do retain many of the nano- to microscale structural features of bone. Hence, their use should be able to provide physiologically-relevant insights into nanoscale mechanical behavior.

2. Materials and methods

2.1. Sample preparation

Adult compact bovine bone from between the tibial metaphysis and diaphysis was cut down to 1.5 mm thick specimens (which was also the approximate thickness of the final samples used for nanoindentation testing) using a diamond-impregnated annular wafering saw (*Buehler*, Isomet 5000) running at 400–600 rpm with constant phosphate buffered saline (PBS, IS = 0.15 M, pH 7.4) irrigation. Longitudinal sections (cut parallel to the long bone axis) were polished down in 2–3 minute intervals using a metallographic polishing wheel (*Buehler*, at ∼100 rpm) and adhesive papers with successively smaller Al_2O_3 particle grit sizes; 9, 3, 1, 0.3, 0.1, and 0.05 μm (*South Bay Technologies*). Samples were rinsed copiously with deionized (DI) water followed by ultrasonicatation in DI water between polishing intervals. Samples were then immediately stored in 20 °C PBS. Demineralization etches were performed using 40% H_3PO_4/60% DI water for 0, 1, 10, 40, and 120 s, followed by at least 48 h of rehydration time in PBS during which time the collagen fibrils to refibrillate [24, 25]. Complete demineralization (confirmed by ash weight) was accomplished by storage in 0.5 M ethylenediaminetetraacetic acid (EDTA) for a minimum of 5 days, where the solution was changed every day. Demineralization produces both large pores on the sample surface as well as internal porosity. Nanoindentation experiments were performed only in the flatter regions between the large surface pores (as determined by optical microscopy). Energy dispersive X-ray (EDX) analysis (probe depth of ∼1 μm) identified only trace amounts of Al (upper atomic percentage limit is 1.5%, *data not shown*).

2.2. Sample characterization: AFM, SEM, GSE, BSE, and Raman spectroscopy

Tapping mode (TM) AFM imaging in ambient environmental conditions was employed using two instruments; (1) a *Veeco Digital Instruments* (DI, Santa Barbara, CA) Multimode SPM IIIA with an AS-130 "JV" piezoelectric scanner and DI NanoSensors TappingMode Etched Silicon Probes (TESP) cantilevers (nominal resonant frequency, $\omega \sim 250$ kHz, nominal spring constant, $k \sim 40$ N/m, and nominal probe tip end radius, $R_{TIP} \sim 10$ nm) and (2) a *Quesant* Q-Scope 350 with Si_3N_4 *Wavemode* NSC16 cantilevers ($\omega \sim 170$ kHz, $k \sim 40$ N/m, $R_{TIP} \sim 10$ nm). The

cantilevers were driven just below ω using a scan rate of 2 Hz and a maximum sampling size of 512×512 pixels. The images reported were amplitude (i.e. cantilever oscillation) and phase (i.e. cantilever phase lag). Amplitude is reflective of surface topography while phase mode is sensitive to many properties such as friction, adhesion, (visco)elasticity, and composition.

Samples were coated with Au-Pd 10 nm thick, and imaged using a JEOL SEM 6320FV. The working distance was 5–7 mm, the sample plane was oriented perpendicular to the electron beam incidence, and a 3 kV accelerating voltage was employed. An environmental SEM (ESEM, *Philips/FEI* XL30 FEG-SEM) was employed for sample characterization in a water vapor environment of uncoated samples. Pressed pellets of 99% pure magnesium oxide (MgO, *Merck*), 99% pure aluminum oxide (Al_2O_3, *Merck*), and 99.99% dense, phase-pure hydroxyapatite [28], undemineralized bone, and acid-treated bone were mounted on the same metal base. Electron acceleration was set to 20 kV with a 184 μA operating current. The working distance was set to 9.6 mm and the water vapor was at 0.4 Torr. Contrast and brightness levels were adjusted and held so that electron images would appear optimally for all samples, allowing for feasible gray level calibration using BSE detection. A gaseous secondary electron (GSE) detector was also placed in the chamber so that secondary electron emissions could be detected to form images of the samples as well.

The mean gray level for BSE images was computed directly from the histogram plot of each substance and compared with that of the other substances. The average atomic number ($\bar{Z}$) for MgO, Al_2O_3, and HA are known respectively to be 10.41, 10.65, and 14.06 where $\bar{Z}$ is given by [29]:

$$\bar{Z} = \frac{\sum(NAZ)}{\sum(NA)} \tag{1}$$

where N is the number of atoms of each element with atomic weight and number A and Z, respectively. Based on the calibration of known substances and the mean gray level obtained from the BSE, it is possible to extrapolate what $\bar{Z}$ is due to the direct relationship between the voltage output from the BSE detector (gray level pixel) and the average atomic number [30–33]. The image analysis software also allows for 2-Dimensional Fast Fourier Transforms (2DFFT) to be taken of images that are 256×256 pixels in size. Gray scale values per pixel were quantified for the images recorded by the BSE detector along with control samples of known $\bar{z}$ where a linear scale was used to approximate the percent weight of mineral content for our samples.

Raman Spectroscopy was used for non-invasive chemical characterization of the undemineralized and acid-etched bone. Through optical microscopy, the *Kaiser Hololab* 5000R Raman Spectrometer was used to record the spectra of Raman shifts. The instrument was operated at 785 nm utilizing Coherent CW Argon/Ion and Ti/S Lasers using a 100 μm diameter optical fiber to maximize throughput.

2.3. Nanoindentation

Nanoindentation experiments were conducted in ambient conditions using a *Hysitron, Inc.* (Minneapolis, MN) Triboindenter equipped with an AFM (*Quesant* Q-Scope) for tapping mode imaging of residual impressions. Indentations were carried out perpendicular to the plane of the Haversian canal axis. The instrument is housed in a granite frame environmental isolation chamber so as to minimize instabilities due to the ambient background noise, with active piezoelectric vibration control stages, and a thermal drift calibration step. Load-controlled nanoindentation was performed using a Berkovich (trigonal pyramid) diamond probe tip. The applied load function was divided into four segments as follows. The first segment consisted of a 3 second(s) hold at zero force in which the probe tip is barely kept in contact with the sample, allowing for tip-sample equilibration. Segment two was a constant loading rate of 9 ± 0.4 μN/s and once the maximum set peak load was reached, the third segment would ensue, which was a hold period of 10–20 s. The fourth segment concluded the experiment with a constant unloading rate of 9 ± 0.4 μN/s. >15 experiments per maximum load were done with each indent at a different sample location. To ensure that creep effects were minimal, three different experiments were conducted. The first was to vary the third hold segment between 10 to 100 s. The second was to use a load function that would, after the hold period, unload to 50% of the maximum force and then reload back to the maximum force for several cycles. The third was to vary the loading/unloading rate by 2 orders of magnitude (the limit of the machine). All three sets of experiments found that the variation in calculated elastic moduli was negligible. Load versus indentation distance curves from multiple experiments using the same maximum load and from different sample locations were averaged and standard deviations calculated and presented on the plots. The tip area function and frame compliance, were calibrated prior to each set of experiments using a fused quartz sample. Values for elastic moduli were calculated from 95% to 20% of the initial unloading curve by fitting these data to contact mechanical theory for an isotropic, elastic half-space (O-P method [23]) using $n = 108$ individual curves. This tip calibration for area function and machine compliance was employed for all of the O-P fits to the experimental data to approximate the elastic moduli. The area between loading and undoading curves was calculated for each force versus distance curve to compute the energy dissipation and a force normalized value was plotted as a function of average maximum load for each case.

2.4. Elastic-Plastic Finite Element Analysis (FEA) of Nanoindentation

A three dimensional elastic-perfectly plastic model was built by FEA using the software package ABAQUS (Hibbitt, Karlsson & Sorensen, Inc.) and solved numerically using the elastic modulus and yield strength as the two fitting parameters. A discussion of the applicability of this model to the samples of interest is given in later sections of this paper. To reduce computational

cost and due to symmetry, 1/6 of the tip and the surface were modeled and the corresponding boundary conditions were applied to ensure the symmetry, i.e. the nodes on the sidewalls were fixed in the direction normal to the sidewall surface (the nodal displacement in this direction is set to be zero). Since the modulus of the diamond probe tip is about 100× higher than the bone and collagen samples studied here, the indenter was modeled as a rigid surface. In practice, the indenter generally does not have an ideally sharp Berkovich geometry; instead it is rounded due to wear and can be characterized by a finite end radius, R_{TIP}, and truncate height, h (which is the distance between the apex of the rounded tip and the apex of the imaginary ideally sharp tip). In order to approximate R_{TIP} and h,nanoindentation experiments were conducted on a standard fused quartz sample. First, a Hertzian elastic sphere-on-a-flat (SOF) model [36] was employed to determine R_{TIP} and h as a function of indentation depth, D, from the experimental nanoindentation data where the modulus of the fused quartz was set to the known value of 72 GPa [37]. These calculations yielded R_{TIP} ∼210 nm at $D \sim 5$ nm and decreased to $R_{TIP} \sim 140$ nm at $D \sim 20$ nm. The spherical geometry and SOF model prediction of R_{TIP} is most accurate for $D < h^2/R_{TIP}$ and for $D > h^2/R_{TIP}$ the SOF model becomes increasingly inaccurate, underestimating R_{TIP} as the geometric transition from spherical to blunted trigonal pyramid (Berkovich) takes place. In order to more precisely determine R_{TIP} and h perfectly elastic FEA simulations were compared to the experimental nanoindentation data using R_{TIP} and h as fitting parameters taking the SOF ranges as the initial starting point for the fits, and yielded $R_{TIP} \sim 180$ nm and h ∼4 nm. Hence, for all subsequent FEA simulations, the indenter was modeled as a rigid surface with Berkovich geometry (inclined face angle, $\beta = 24.7^\circ$, apex angle, $\gamma = 77.1^\circ$) having R_{TIP} of 180 nm and truncate height of 4 nm. The samples were modeled using an 8-node linear brick element hybrid with constant pressure (C3D8H in ABAQUS element library). The mesh was refined in the vicinity of the contact region where large gradients in stress and strain prevail. Several mesh densities were analyzed and an optimal mesh was finally chosen for use in all simulations which contained 6195 nodes and 5491 elements. The element size increased with increasing distance from the indentation axis and surface. Large deformation theory and frictionless contact between the indenter and material were assumed throughout the analysis. A smaller number of individual experimental nanoindentation curves were fit ($n = 3$) compared to the O-P method due to the longer time and computational cost required for the FEA simulations.

3. Results

3.1. Sample characterization by SEM, GSE, BSE, AFM, and Raman spectroscopy

The microstructure of the undemineralized bone samples as revealed through SEM (Fig. 1(a)) showed a rough surface morphology with no obvious periodic or directional trends [38]. The underlying fibrous nature of the matrix is revealed in Fig. 1(b) through SEM of a fractured surface edge crack which presumably show mineralized collagen fibrils. A higher resolution TMAFM image taken in ambient conditions (Fig. 1(c)) shows a similar surface morphology with topographical features ∼10 nm in height and 51.0 ± 30.7 nm in lateral dimension and no preferred orientation or banding structure as assessed by a 2DFFT of this image (Fig. 1(d)). The lateral topographical feature size measured here correlates well with the size of the mineral particles observed by AFM [10, 11], TEM [2], and XRD [39]. The apparent lack of the characteristic collagen fibril banding is expected as a significant amount of mineral is expected to be located outside of the collagen fibrils [40], thus obscuring the distinct banding [11, 41]. Fig. 1(e) is a larger scan size BSE image, which possesses lighter gray level values (indicative of higher degrees of mineralization) throughout the sample at localized regions that run between channels where Haversian canals are located [16]. Calculations from Fig. 1(e) yielded ∼58 wt% mineral content. The Raman spectrum in Fig. 1(f) has peaks which denote bands characteristic of the mineral in bone [35]. Porosity and mineral content are within expected ranges [7].

Fig. 2(a) is an SEM micrograph of the bone sample which had been etched for 120 s in H_3PO_4 and shows a distinct layer of collagen fibrils on the surface, with a preferred orientation of the fibril axis in the plane of the sample, as well as the 67.8 ± 8.8 nm characteristic banding periodicity (Fig. 2(b)). Interlocking of fibrils was observed in TMAFM images as shown in Fig. 2(c). The average fibril diameter was found to be 151.0 ± 16.9 nm with parallel banding lines oriented at an angle of ∼10° to the collagen fibrillar axis. Uniformly distributed on top of the surface of the fibrils, there also appears to be softer (in many cases likely deformed by the probe tip during imaging) tiny globular structures (size ∼10 nm) present that can be attributed to non-collagenous proteins. A 2DFFT (Fig. 2(d)) of TMAFM images similar to Fig. 2(c) but with larger scan sizes similar to that shown by SEM (Fig. 2(a)) agrees with the data in Fig. 2(b). The relatively dark BSE gray levels shown in Fig. 2(e) indicate that the mineral content (∼4 wt%) is significantly lower compared to the undemineralized bone sample Fig. 2(f) confirms peaks which denote bands characteristic of the mineral in bone [36].

Fig. 3 shows BSE images that exhibit the full range of mineralization from the phase pure HA (Fig. 3(a)) to the completely demineralized bone (Fig. 3(e)). The etched samples had mineral contents of ∼37 wt% (1 s etch), 26 wt/% (10 s etch), ∼19 wt% (40 s etch), ∼4 wt% (120 s etch), which was determined by the etch time. All bone samples that were subjected to the demineralization etch exhibited the same type of fibrillar banding structure found in Figs. 2(c) and 3(f).

3.2. Nanoindentation and elastic contact mechanical analysis

Averaged nanoindentation curves on loading and unloading are shown in Fig. 4 for the various samples up to maximum loads of ∼1000 μN. All samples

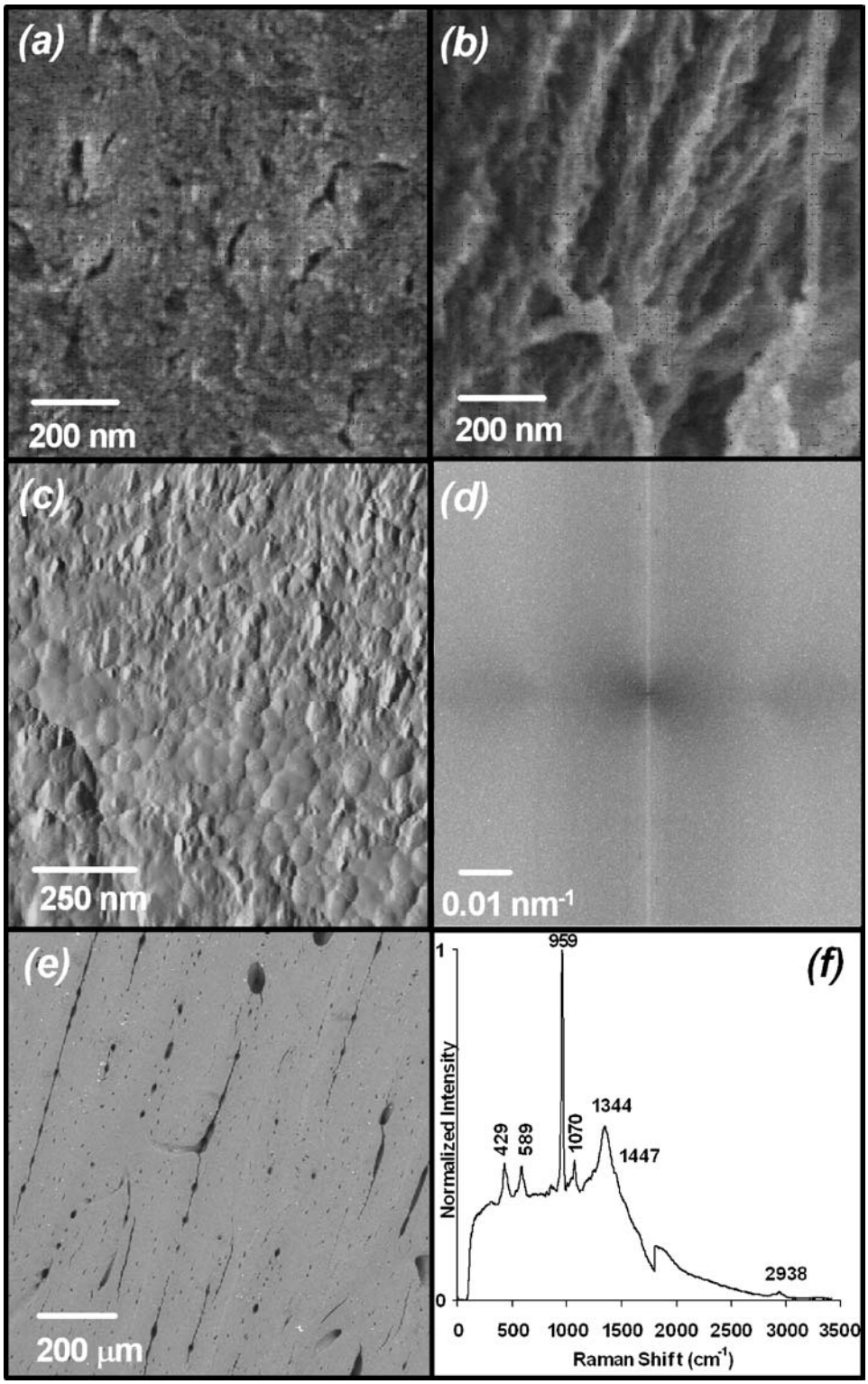

Figure 1 Characterization of an undemineralized longitudinal section of adult bovine tibial cortical bone; (a) Scanning electron microscopy (SEM) image shows a ∼10% porosity with irregular, granular-type surface features, (b) SEM image showing the edge along a fracture surface, revealing rough fibrous material indicative of mineralized collagen fibers, (c) Tapping mode atomic force microscopy (TMAFM) image in air (taken with *Veeco DI Multimode*) showing surface morphology at higher resolution, (d) 2D Fast Fourier Transform (FFT) of (c), which does not exhibit any noticeable peaks, (e) low vacuum, micron-scale (back-scattered electron) BSE image in water vapor, and (f) Raman spectrum for sample (e). Peaks can be observed at specific wavenumbers that are characteristic for bone (cm^{-1}); 589 ($PO_4^{3-}\nu_4$), 959 ($PO_4^{3-}\nu_1$; P─O symmetric stretch), and 1070 ($CO_3^{2-}\nu_1$; CP─O in plane stretch). There is a noticeable jump in the overall background intensity relative to the observed peaks, due to proteins, which fluoresce.

exhibited mechanical hysteresis at each load tested. The loading responses exhibit significant changes in mechanical behavior shown in the shape of the overall loading and unloading response as the mineral content was varied. Particularly, the initial unloading slope, dP/dh, of the unloading curve and the residual depth of impression vary markedly. The individual nanoindentation curves were relatively smooth with no discontinuities or distinct changes in slope apparent (*data not shown*). The O-P fits yielded average elastic moduli that ranged from 12.86 ± 2.9 (∼58 wt% mineral content) to 1.91 ± 0.12 GPa (∼0 wt% mineral content) (Fig. 5(a),

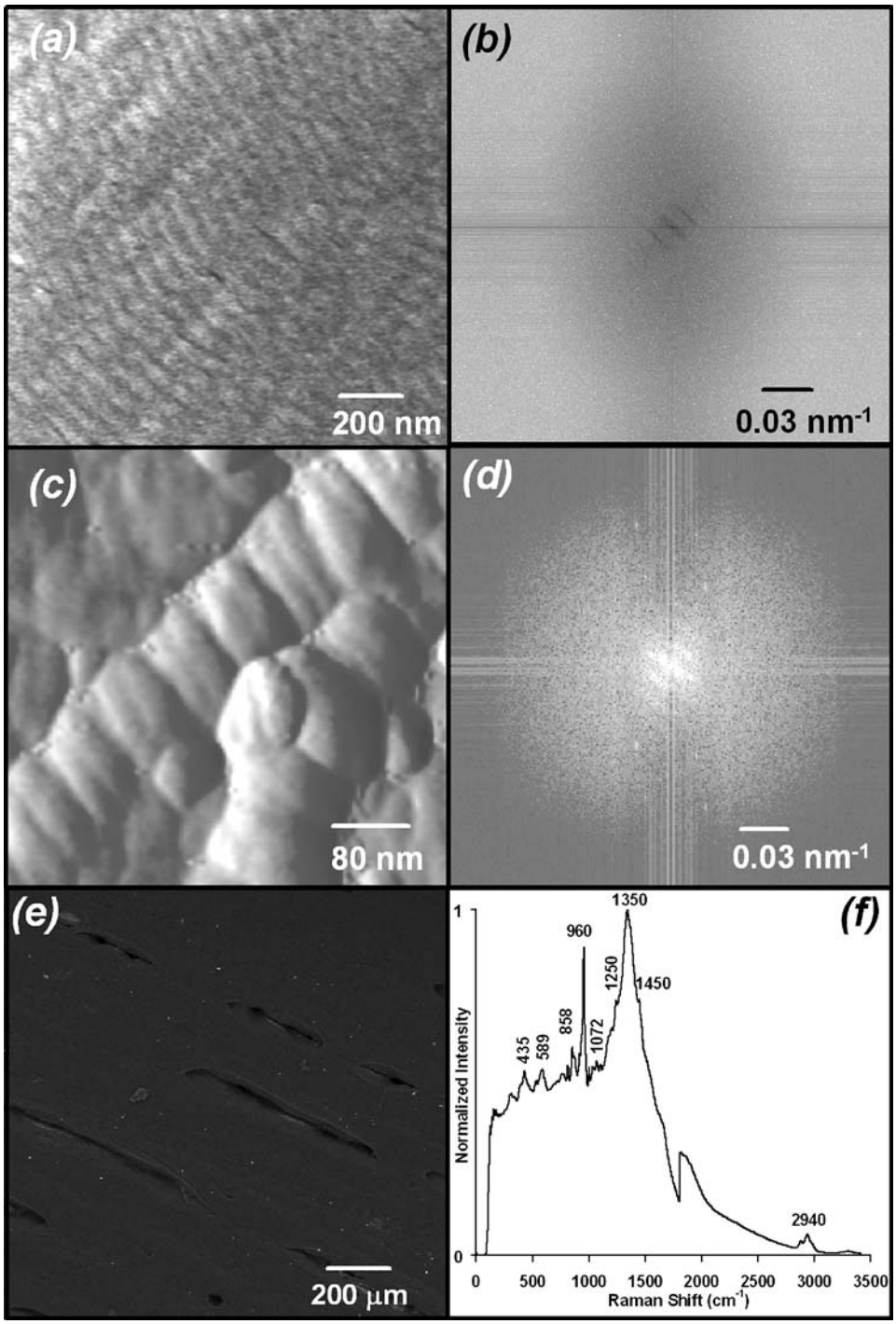

Figure 2 Characterization of an H_3PO_4-treated (∼4 wt% mineral content) longitudinal section of adult bovine tibial cortical bone; (a) Scanning electron microscopy (SEM) image, (b) 2D Fast Fourier Transform (FFT) of (a) which exhibits the known characteristic axial banding periodicity of 67 nm for type I collagen fibrils, (c) higher resolution TMAFM amplitude image in air (taken with *Veeco DI Multimode AFM*), (d) 2DFFT of TMAFM image similar to that show in (c) but with a larger scan size, which shows the expected 67 nm axial periodicity, (e) low vacuum micron-scale (back-scattered electron) BSE image in water vapor, and (f) Raman spectrum. The peak at 1447 (CH_2 wag) cm^{-1} denotes a typical organic presence. The Raman spectrum shows a good deal of fluorescence due to a greater percentage of protein in the sample compared to the smaller "mineral" peaks.

diamond symbols and Table I). Fig. 5(b) shows the relation of the energy dissipation as a function of the maximum force exerted by the indenter tip on the undemineralized and ∼4 wt% mineral content samples. Comparing the two ratios, the undemineralized bone has less of an energy dissipation to maximum load ratio as the maximum force increases. For the maximum load of 900 μN, average values for the acid-treated bone compared with that of the undemineralized bone were statistically very different (>0.999 t-percentile).

3.3. AFM imaging of indented regions

Fig. 6(a) is a TMAFM image (*Q-scope*) of the indented region of the undemineralized bone sample. Residual deformation is clearly visible localized within the indent region with no apparent deformation of the material away from the indent region or any signs of brittle microcracks. The surface topographical features have been flattened within the indent region and there is an appreciable amount of feature consolidation and material pileup at the edges of the indent region. For

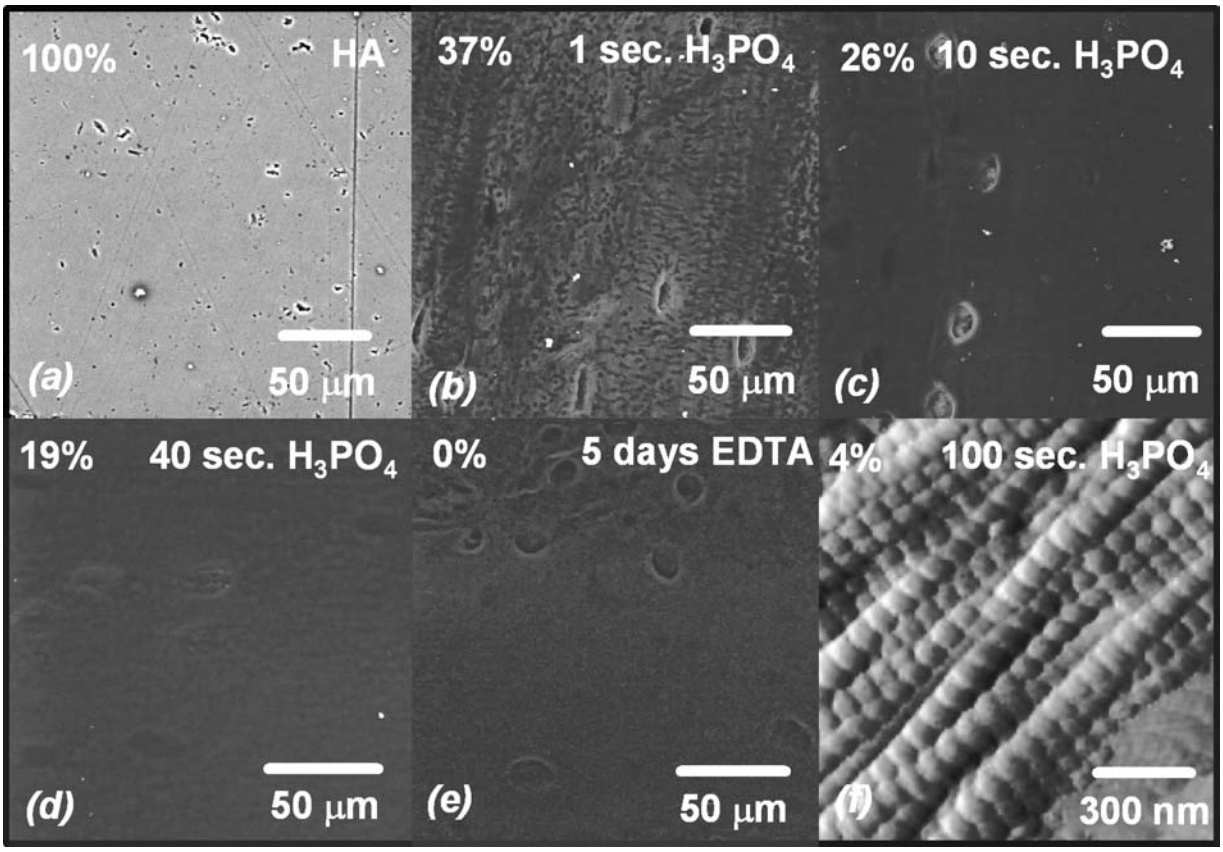

Figure 3 Characterization of longitudinal sections of adult bovine tibial cortical bone with different mineral contents. Back-scattered electron (BSE) images; (a) phase-pure synthetic HA (100 weight(wt%) mineral content), (b) 37 wt% mineral content, (c) 26 wt% mineral content, (d) 19 wt% mineral content, and (e) 0 wt% mineral content. (f) Typical type I collagen fibrillar banding structure observed under higher resolution TMAFM (amplitude image in air using *Veeco DI Multimode AFM*).

the ∼4 wt% sample at a maximum load of 300 μN (Fig. 6(b)), collagen fibril banding was still clearly visible in areas within the indent regions, while at a higher maximum load of 700 μN (Fig. 6(c)) much of the indented area had lost its characteristic banding (mechanical denaturation). For the lower maximum load of 300 μN, discontinuities and kinking along the axial fibril direction were visible within the indented region. For both maximum loads, a tortuous curved, path was visible along the tip apex lines which appeared to slice through the thickness of the collagen fibrils. At the higher maximum load of 700 μN (Fig. 6(c)), a crack was observed to continue outside of the indented region in the same direction as the tip apex lines. Other similar cracks were observed outside the indented region and appeared to be due to failure of interfibril interfaces. Figs. 7 (a) and (b) are AFM images of the ∼4 wt% mineral content samples deformed to higher loads of 1000 and 7000 μN, respectively, taken 3 hours (h) post-indent and show more extensive mechanical denaturation of collagen fibrils, in particular at the apex of the indent where the greatest pressure is applied. Fig. 7(b) exhibits an interesting 3-lobed, amorphous, unbanded region which follows the probe tip apex lines.

TABLE I Modulus and yield stress values as calculated by the Oliver-Pharr (O-P) method and finite element analysis (FEA) for adult bovine tibial cortical bone samples of varying degree of mineralization

Wt% mineral content	E GPa (O-P)	E GPa (FEA)	σ_y GPa (FEA)
58	12.9 ± 2.9	9.0 ± 0.35	0.24 ± 0.1
37	7.9 ± 2.7	4.6 ± 0.7	0.08 ± 0.04
26	3.0 ± 0.5	2.2 ± 0.6	0.16 ± 0.03
4	3.8 ± 0.7	2.0 ± 0.4	0.11 ± 0.08
0	1.9 ± 0.1	1.9 ± 0.6	0.07 ± 0.03

3.4. Elastic-plastic FEA simulations of nanoindentation

The significant amount of residual deformation observed by AFM imaging (Fig. 7) is likely due to a combination of viscoelastic and plastic deformation. Since it was observed by AFM imaging that the indentation impression did not disappear after a number of hours upon removal of the indentation load, there is a relatively long recovery time for the viscoelastic component of the deformation. In macroscopic uniaxial tension and compression tests of bone, the onset of plastic deformation is characterized as a distinct slope change in the stress-strain curve, i.e. the yield stress, σ_y, followed by a plastic region typically with a small amount of strain hardening, depending on the type of bone [19, 42, 43]. The purpose of the numerical modeling portion of this paper is to use a simple constitutive model to characterize the nonlinear nano- to micromechanical behavior of bone and to approximate the local material properties such as the elastic modulus and yield strength. Hence, FEA simulations were conducted using a stress-strain relation in the form of

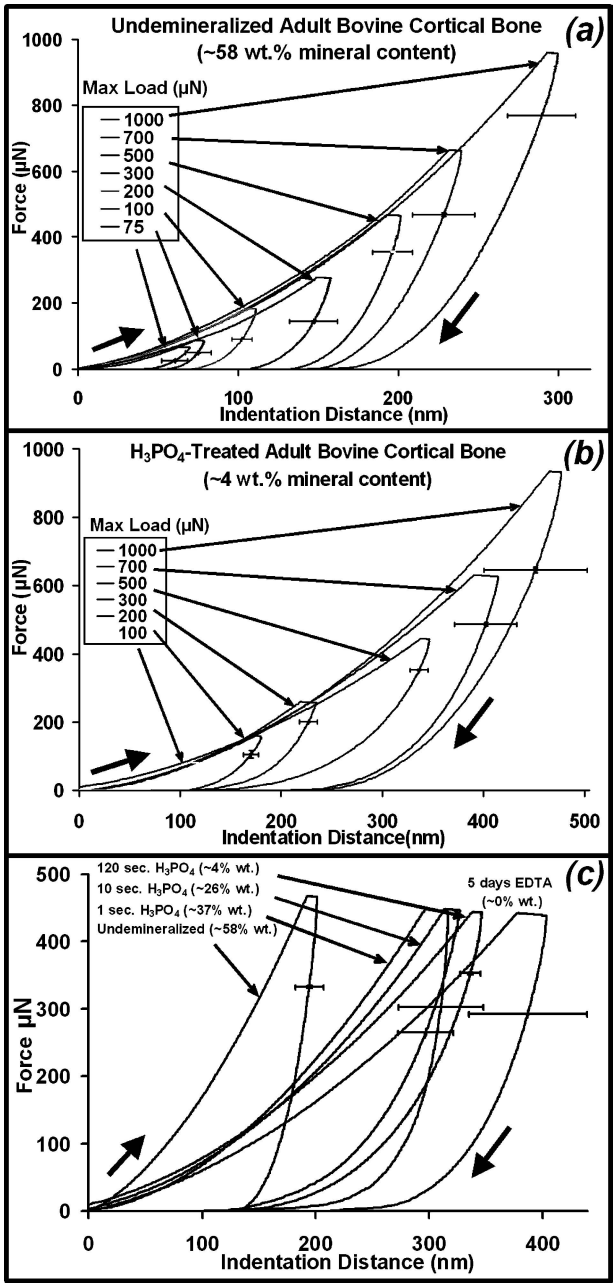

Figure 4 Average nanoindentation curves for adult bovine tibial cortical bone on loading and unloading; (a) undemineralized and (b) partially demineralized samples, both as a function of maximum load. (c) A comparison of the nanoindentation data for a maximum load of 500 μN for samples of varying mineral content. The inset labels "wt%" in the plots refer to the weight percent mineral content.

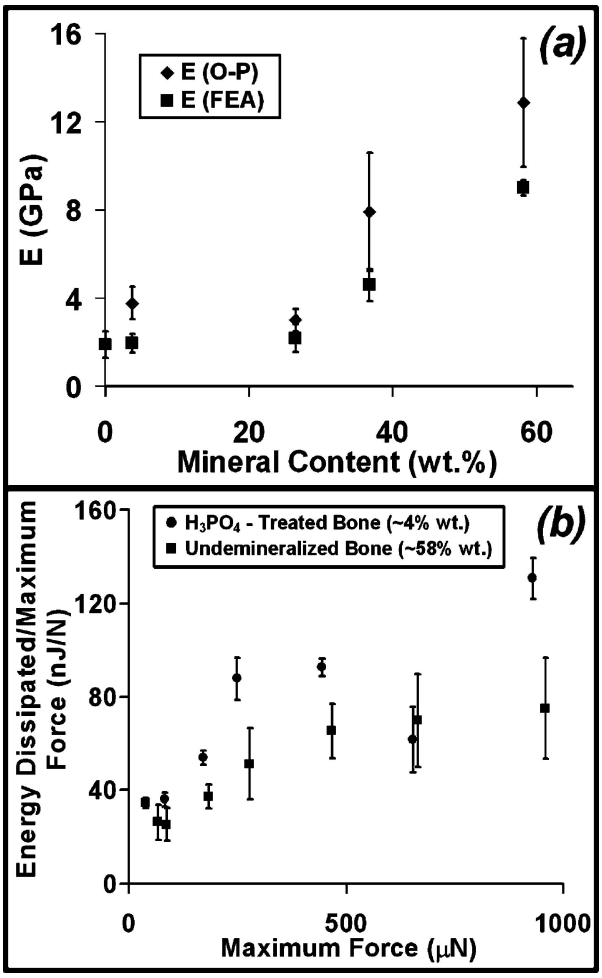

Figure 5 Plots for adult bovine tibial cortical bone of (a) elastic modulus values calculated from the fits to the Oliver-Pharr (O-P) method and finite element analysis (FEA) simulations, as a function of the weight (wt)% mineral content estimated from BSE which are also detailed in Table 1. The O-P moduli values are averages obtained from all nanoindentation curves (at all maximum loads) while FEA fits were done to nanoindentation curves taken using maximum loads of 1000 μN. Student t-tests revealed statistically significant differences in stiffness the undemineralized bone compared to the other samples. (b) Normalized energy loss as a function of maximum load. The inset labels "wt%" in the plot refers to the weight percent mineral content.

an elasto-perfectly plastic model, which is intended to approximate the stress-strain behavior demonstrated in macroscopic mechanical tests [44]. Here, we refer to "plastic" as residual deformation due to a combination of permanent and viscoelastic deformation. One justification for using an elastic-plastic model to describe the nanomechanical behavior of these samples is the long recovery time observed for deformation. In addition, recent studies [46] have shown that the effect of time-dependence during typical nanoindentation experiments in cortical tibial bone is minimal as evidenced by the fact that as the indentation rate was varied by 100× the energy dissipation due to plasticity varied by <10%. In this previous work [46], it was also observed that when the time segment in between loading and unloading held at maximum load was increased by 100×, the energy dissipation varied by <10%. The elastic-plastic model thus provides a simple constitutive model with minimal material parameters (two). Other constitutive models which incorporate large deformation viscoelastic or viscoplastic behavior require an additional two or more material parameters, thus reducing confidence in the fits.

As the nanoindentation tests conducted in this paper contain ∼30 collagen fibrils laterally and ∼3 collagen fibrils vertically with the contact area, as a first approximation the sample was modeled as a homogeneous material. More refined FEA models which take into account the mechanical properties of the mineral and organic constituents, anisotropy due to local orientation of the collagen fibrils, viscoelasticity, and structural heterogeneity are currently under development. Fig. 8(a)–(c) show FEA fits to the averaged nanoindentation data for the undemineralized sample, ∼4 wt% mineral content sample, and the completely demineralized sample,

respectively. The elastic-plastic model captures both loading and unloading behavior reasonably well. The most important regions for fitting the two parameters were the initial unloading slope and the residual plastic indentation depth. Fig. 5(a) shows the FEA fitted results for the moduli compared to the O-P method as a function of weight percent mineral content. The FEA simulations predict moduli values 21–48% lower than the O-P method, but display a similar trend with mineral content. From the evidence of pileup shown in Fig. 6(a), the O-P prediction most likely underestimates the true contact area, resulting in an overestimation of the Young's modulus. T-test results revealed the difference between the ∼0 wt% and ∼58 wt% samples to be statistically significant (percentile >0.995). Fig. 9(a) shows the yield strengths predicted from the FEA simulations as a function of mineral content and give $\sim 0.30 \pm 0.09$ GPa for undemineralized bone, and ∼0.07–0.2 GPa for the partially demineralized samples. Student t-test shows a >0.95 percentile statistical difference for comparisons between the completely demineralized and undemineralized bone. Figs. 9(b) and (c) show the mesh that was formulated in the FEA to carry out the simulation.

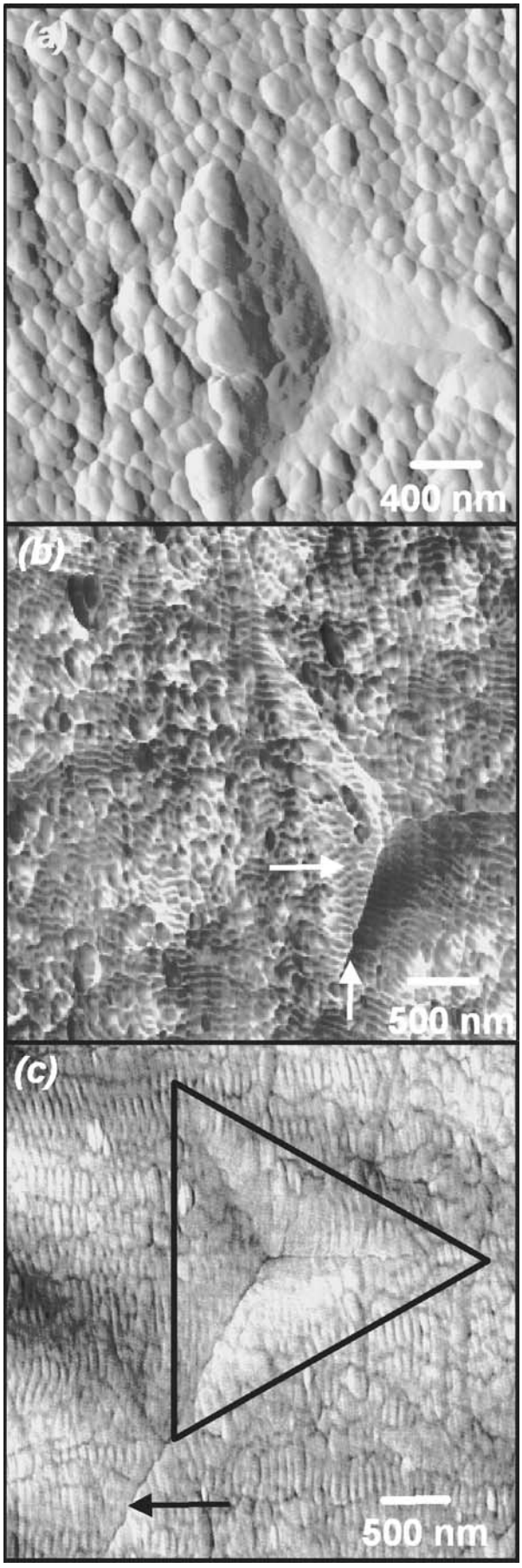

4. Discussion

Coarse positionally-specific nanoindentation experiments in conjunction with optical microscopy on human femoral and vertebral cortical bone in air at relatively large loads up to ∼20 mN and ∼1 μm depths have been reported in the literature and shown variations in nanomechanical properties for different types of bone (e.g. interstitial, osteonal, etc.) [47], with age [47], orientation [14, 48], and location (e.g. distance from osteonal center) [9, 16]. In a related study, high maximum load indentations (∼15 mN) were performed on articular calcified cartilage and subchondral bone of post mortem and osteoarthritic femoral heads at locations of varying degrees of mineralization [18]. Modulus values for cortical bone predicted from the O-P method in these studies ranged between ∼15–25 GPa, similar to that reported for tensile macroscopic mechanical properties [49].

4.1. Moduli

Values for average moduli estimated by fits to both elastic and elastic-plastic models for the undemineralized bone (∼12.9 GPa, ∼7 GPa, respectively) are somewhat less than that experimentally reported by nanoindentation for the same direction for dehydrated and embedded human tibial cortical bone (16.6–17 GPa) [50]. Here, the authors apply a rule of mixtures

Figure 6 Tapping mode atomic force microscopy (TMAFM) images of residual indentations of adult bovine tibial cortical bone (taken with a *Quesant* AFM attached to a *Hysitron* nanoindentor approximately 15 minutes following indentation in ambient conditions); (a) amplitude image of undemineralized sample indented to a maximum load of 700 μN, (b) phase image of a partially demineralized sample (4 wt% mineral content) indented to a maximum load of 300 μN. The inset arrows show that the kinked collagen fibrils maintain their banded structure within the residual indent region, (c) phase image of the 4 wt% mineral content sample indented to a maximum load of 700 μN. The image shows disruption of fibril interfaces and a tortuous path along the tip apex lines compressing and slicing through collagen fibrils. The inset arrow shows crack formation along the edge of the residual impression.

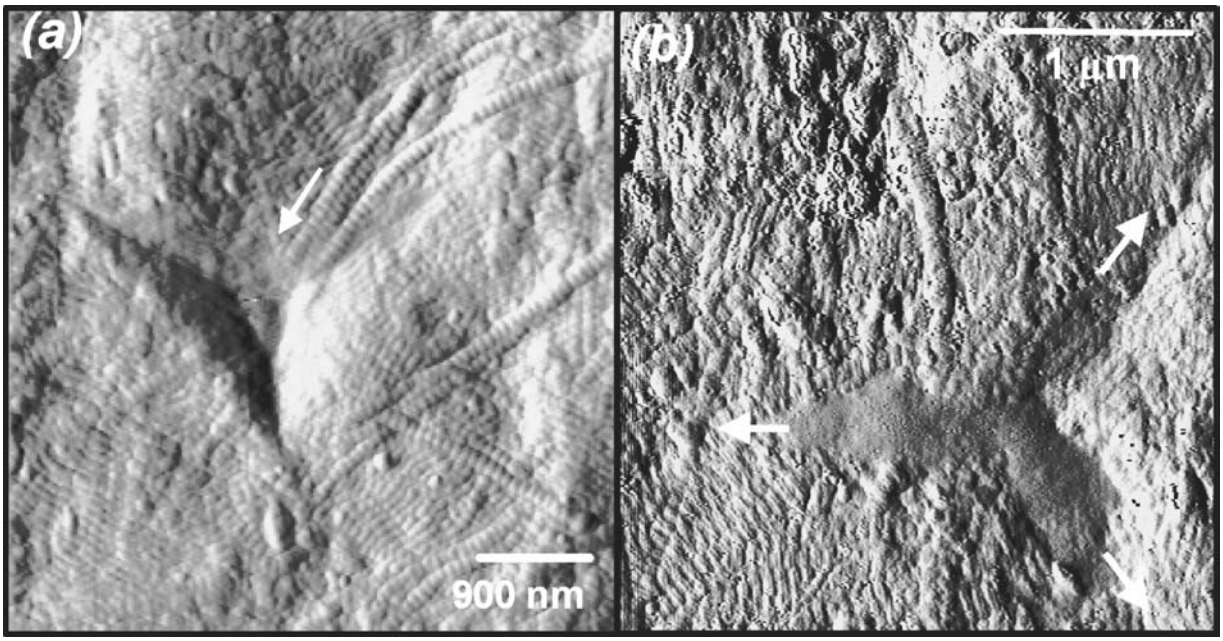

Figure 7 High resolution tapping mode atomic force microscopy (TMAFM) amplitude images in ambient conditions of residual indents of partially demineralized adult bovine tibial cortical bone (4 wt% mineral content) taken 3 hours after indentation (*Veeco DI Multimode* AFM); (a) The indent was made using ∼1000 μN maximum load. The arrow shows the path of collagen fibrils that lose their supramolecular banding structure near the tip apex. Along the outside, where the force is significantly lower, the fibrils merely flatten out from the sink-in deformation. (b) The indent was made using a ∼7000 μN maximum load. The middle indent region is shown where the arrows mark the apex lines of the indenter.

correction to take into account osteonal, interstitial, and void volume fraction and assume a 15% artificial increase in modulus due to ethanol dehydration (used in the sample preparation process) yielding corrected moduli values of 14.4–14.9 GPa. These reported values may differ from those obtained in this study due to additional stiffening from ethanol dehydration, higher maximum loads up to 20 mN covering greater contact areas, faster loading rates of 1 mN/sec, and the different species of bone used [14–16, 47, 48].

The average moduli values calculated from both elastic and elastic-plastic models for the undemineralized sample were found to exceed the other samples by up to ∼6×, which is consistent with the trend for macroscopic tensile modulus of cortical bone known increase with the mineral content [51]. XRD studies show that acid demineralization leads to both an averaged reduction in the mineral crystallite size as well as the lattice microstrain in bone [52]. Internal porosity is also likely. As in macroscopic mechanical property measurements, it should be stated that trends with mineral content observed here are likely to be complicated by other structural and chemical changes in the distribution and location of mineral, the organic-mineral interface, and the physiochemical properties of collagen.

4.2. Yield strength

The yield strengths, σ_y, predicted from the FEA simulations are $\approx\frac{1}{8}$ to $\frac{1}{24}$ of the FEA-determined elastic moduli, E, which are higher than those obtained in macroscopic mechanical testing tests [19]. For example, a survey of 39 bones from 22 species found that $\sigma_y \approx \frac{1}{120}E$ to $\frac{1}{140}E$ [19]. σ_y obtained from fits to nanoindentation data have been observed to exceed those measured by macroscopic mechanical measurements for other types of other materials as well [53]. Possible reasons for this observation are a decreased number of defects as the volume of material deformed becomes smaller and/or pressure-induced hardening (increased yield strength) due to the increasing internal resistance for damage to develop as the pressure increases [17] (discussed further in the next section).

4.3. Nanoscale mechanisms of deformation and energy dissipation

As described in the Introduction section, yielding and the resulting high toughness of bone has been attributed to a variety of deformation mechanisms that take place at multiple length scales. Our AFM imaging results of the partially demineralized bone (Figs. 6(b, c), and 7) show that collagen fibril lateral curvature and normal flattening can be achieved while still maintaining the collagen banding structure indicative of the native supramolecular structure at lower loads (∼300 μN). This finding is consistent with AFM studies on collagen fibrils in tendon [54] and supports the idea of an adaptable, compliant fluid-like fibril structure [55]. Kinking along the axial direction observed here is also consistent with previous studies [54]. Interestingly, at the highest applied indentation loads, mechanical denaturation of collagen fibrils is observed (Fig. 7) taking place close to the junction edge of the two faces of the indenter, which is the region found to have the highest plastic deformation as revealed by FEA simulations (Fig. 8b).

In the undemineralized bone samples (Fig. 6(a)), a dramatic near complete elimination of surface topographical features is observed which could be indicative of the pressure induced structural transition of bone mineral previously mentioned [56]. While it was not

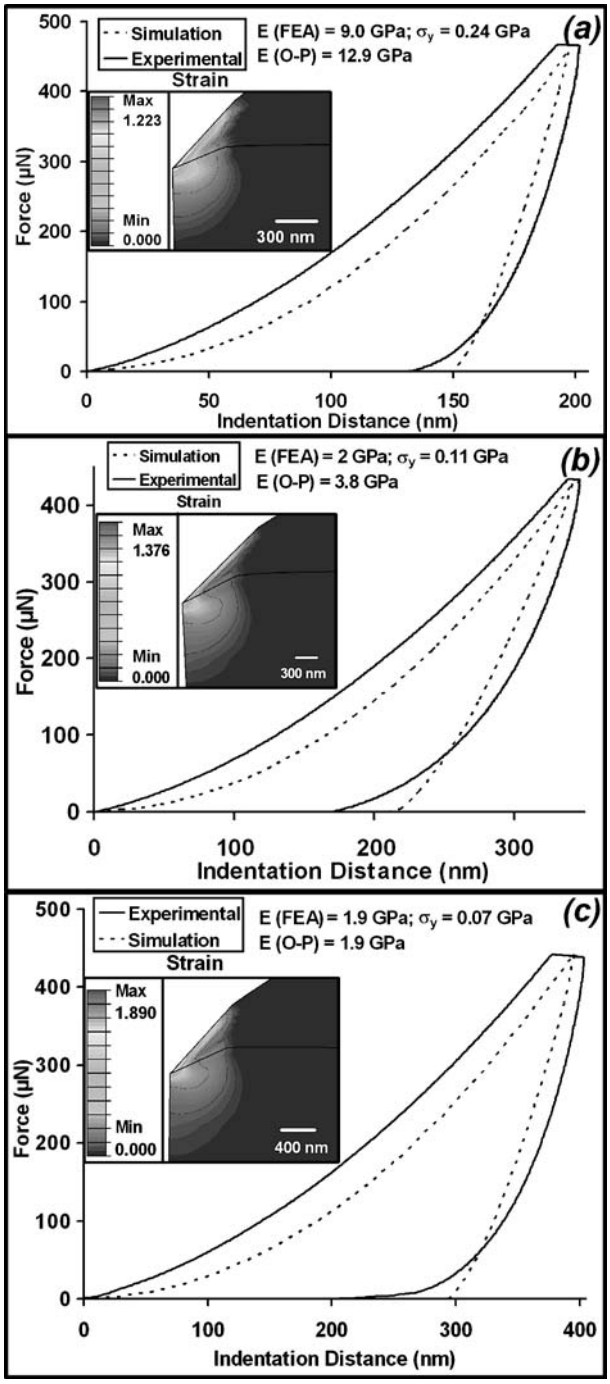

Figure 8 Plots which show a comparison between the experimental nanoindentation data and the finite element analysis (FEA) simulations for; (a) undemineralized bone, (b) partially demineralized bone (∼4 wt% mineral content), and (c) fully demineralized bone. Inset represents contour plots for the simulated plastic strain.

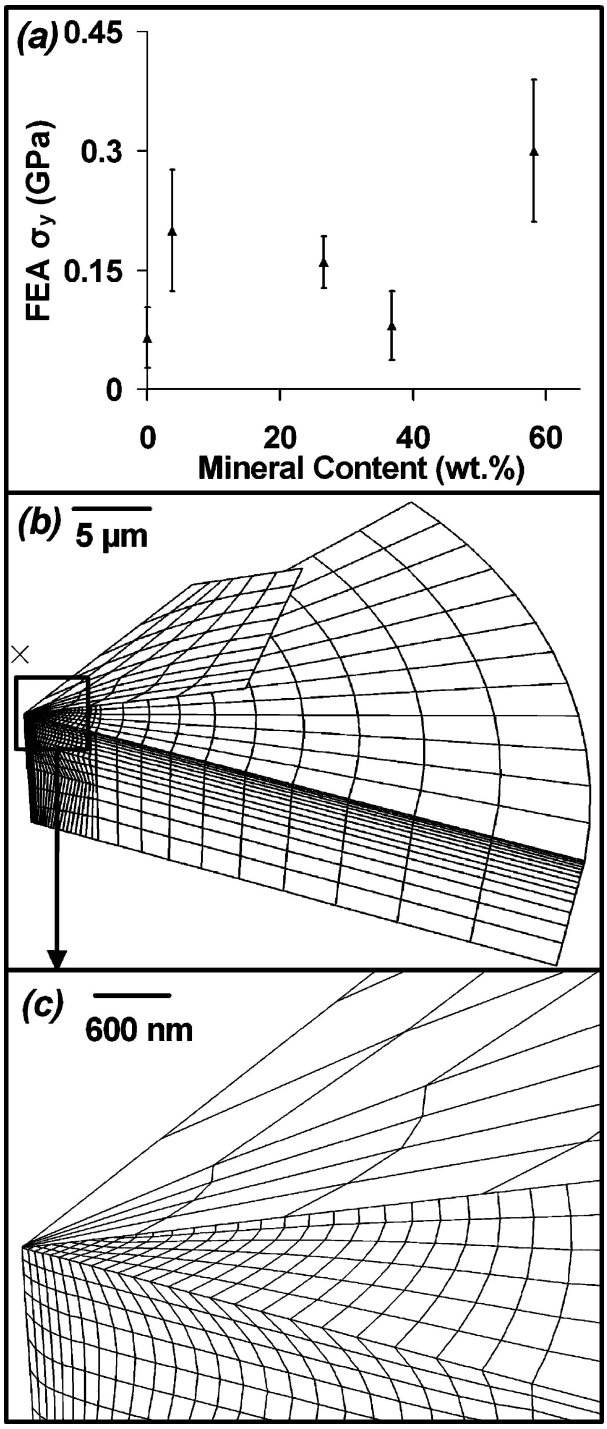

Figure 9 (a) Finite element analysis (FEA) fits for the yield stress, as a function of weight (wt%) mineral content for adult bovine tibial cortical bone. The one sixth homogeneous mesh plot for FEA simulation is shown in (b). (c) A closer view of the finer mesh where the majority of strain occurs.

possible to observe denaturation of collagen fibrils in the undemineralized sample (since the collagen banding was not visible in the undeformed sample Fig. 6(a)), it can not be ruled out as well. FEA simulations reveal that at an indentation depth of 280 nm (maximum load of 1000 μN) the highest pressure is about 520 MPa, which is close to the pressure required for phase transition in sintered synthetic dense HA [56]. In addition to the high pressure, the material is also subjected to high shear stress; the FEA simulation shows the highest equivalent shear stress to be about 140 MPa, which can initiate plastic deformation of HA plates, as well as expedite the phase transition due to increased lattice energy when the material is subjected to shear stress. Although displacement of individual mineral particles could not be resolved, the occurrence of extensive viscoelastic/plastic deformation and collagen denaturation suggests that this is likely. Analogously, micromechanics studies of a rubber filled thermoplastic composite system show that the plastic deformation of thermoplastic results in the displacement of particles after unloading [57, 58].

The yielding mechanism is also susceptible to retardation by pressure, which leads to an increased yield

stress observed in nanoindentation. For instance, the slippage between collagen fibrils and themselves and/or mineral particles is expected to be retarded by the pressure because of increasing resistance to the relative motions. Microcracks, if they exist, also are subjected retardation because the applied pressure tends to close these cracks, requiring a higher stress to propagate the cracks resulting in a higher yield stress.

As shown in Figs. 4(d) and 5(b), the partially demineralized bone exhibits the highest ductility and dissipates the most energy at all maximum forces tested. One explanation for this result, in particular when comparing to the undemineralized bone, is the possibility of underlying porosity and voiding, which would relieve triaxial stresses, and facilitate plastic deformation via for example, increased molecular mobility and mineral displacement mechanisms. Differences in the collagen supramolecular structure and water content (which are unknown) are also likely to have a significant impact on the energy dissipation.

5. Conclusions

In this paper, a multitechnique experimental and numerical modeling methodology was employed for studying the nanomechanical properties and detailed ultrastructural deformation mechanisms of bone. Bovine tibial cortical bone samples of known and varied mineral content (∼58%, ∼37%, ∼26%, ∼4%, and ∼0 wt%) were prepared, characterized, tested by nanoindentation with the loading direction perpendicular to the osteonal axis, and analyzed *in-situ* and *post-mortem* by high resolution AFM imaging. Mineral content was found to have a significant effect on both the nanoscale mechanisms of deformation and nanomechanical properties. A 2–6× increase in modulus was observed for the ∼58 wt% sample (∼7–12 GPa) compared to the ∼0 wt% sample sample. Upon inspection, all samples exhibited similar values for work of plastic deformation. The yield strength predicted by FEA simulations was found to have a very slight dependence on the mineral content. The partially demineralized samples underwent collagen fibril deformation and kinking without loss of the characteristic banding structure at low maximum loads (∼300 μN). At higher maximum loads (greater than ∼700 μN) mechanical denaturation of collagen fibrils was observed within the indent region, as well as disruption of interfibril interfaces and slicing through the thickness of individual fibrils leading to microcracks along the tip apex lines and outside the indent regions. For the undemineralized ∼58 wt% mineral content sample, the near complete elimination of surface topographical features provided evidence for plastic deformation via the mechanism of a pressure induced structural transition of the mineral component observed at loads as low as 300 μN and displacements of 100 nm. The FEA elastic-plastic continuum model was able to predict the nanomechanical behavior of the differently mineralized samples reasonably well on loading and unloading suggesting applicability at the length scales probed in this study. While the O-P method yields immediate quick results in a simple and effective manner, it tended to overestimate the elastic moduli by 21–48% as compared to the FEA simulations at the nanoscale which still require better models for predictive accuracy.

Acknowledgments

The authors would like to thank the Cambridge-MIT Institute, the Whitaker Foundation, and the U.S. Army through the MIT Institute for Soldier Nanotechnologies (Contract DAAD-19-02-D0002) with the U.S. Army research office for funding. The content does not necessarily reflect the position of the government and no official endorsement should be inferred. Also, the Center for Materials Science and Engineering at MIT facilities, Professor Krystyn van Vliet for helpful discussions, Alan Schwartzman and the MIT Nanomechanical Technology laboratory, and Professor William Bonfield (Cambridge University, UK) for providing synthetic hydroxyapatite samples.

References

1. R. LAKES, *Nature* **361** (1993) 511.
2. W. J. LANDIS, *Bone* **16** (1995) 533.
3. J. Y. RHO, L. KUHN-SPEARING and P. ZIOUPOS, *Med. Eng. Phys.* **20** (1998) 92.
4. S. WEINER and H. D. WAGNER, *Ann. Rev. Mater. Sci.* **28** (1998) 271.
5. R. M. BILTZ and E. D. PELLEGRINO, *J. Bone Joint Surg.*, **51-A** (1969) 456.
6. S. MANN, in "Biomineralization: Principles and Concepts in Bioinorganic Materials Chemistry" (Oxford Chemistry Masters Series, 2001) p. 89.
7. M. NORDIN and V. FRANKEL, in "Basic Biomechanics of the Musculoskeletal System" (Lea & Febiger, Philadelphia, 1989) p. 3.
8. J. Y. RHO and G. M. PHARR, in "Mechanical Testing of Bone and the Bone-Implant Interface," edited by Y. H. An and R. H. Draughn (CRC Press, Boca Raton, FL, 2000) p. 257.
9. S. HENGSBERGER, A. KULIK and Ph. ZYSSET, *Euro. Cells Mater.* **1** (2001) 12.
10. S. J. EPPELL *et al*., *J. Orthop. Res.* **19** (2001) 1027.
11. T. HASSENKAM *et al*. *Bone* **35** (2004) 4.
12. V. BARANAUSKAS *et al*., *J. Vac. Sci. Technol. A* **19** (2001) 1042.
13. J. THOMPSON *et al*., *Nature* **414** (2001) 773.
14. J. Y. RHO *et al*., *J. Biomed. Mater. Res.* **45** (1999) 48.
15. J. Y. RHO, T. Y. TSUI and G. M. PHARR, *Biomaterials* **18** (1997) 1325.
16. J. Y. RHO *et al*., *Bone* **25** (1999) 295.
17. Z. FAN, J. SWADENER, J. RHO, M. ROY and G. PHARR, "Anisotropy Nanoindentation Properties of Human Cortical Bone," Transactions of the Annual Meeting of the Orthopaedic Research Society (San Francisco, CA, 2001) vol. 26, paper no. 0525.
18. V. L. FERGUSON, A. J. BUSHBY and A. BOYDE, *J. Anatomy* **203** (2003) 191.
19. J. D. CURREY, *J. Biomech.* **37** (2004) 549.
20. L. K. BACHRACH *et al*., *J. Clin. Endocrin. Metabol.* **84** (1999) 4702.
21. K. J. BUNDY, in "Bone Mechanics," edited by S. C. Cowin (CRC Press, Boca Raton, Florida, 1989) p. 197.
22. S. C. COWIN, in "Bone Mechanics," edited by S. C. Cowin (CRC Press, Boca Raton, Florida, 1989) p. 98.
23. W. C. OLIVER and G. M. PHARR, *J. Mater. Res.* **7** (1992) 1564.
24. F. E. FENINAT *et al*., *J. Biomed. Mater. Res.* **42** (1998) 549.
25. D. P. NICOLELLA *et al*., "Ultrastructural Characterization of Damaged Cortical Bone Using Atomic Force Microscopy," in

Proceedings of the 1999 American Society of Mechanical Engineering (ASME) Bioengineering Conference: Big Sky, Montana, 1999.
26. S. S. SHEIKO and M. MOLLER, *Chem. Rev.* **101** (2001) 4099.
27. S. HENNING *et al*., in Augustusburg Conference of Advanced Science, Augustusburg, Saxony, Germany, October 11–13, 1999. Weblink: http://www1.medizin.unihalle.de/biomechanik/acas99/abstracts/henning.htm.
28. M. AKAO, H. AOKI and K. KATO, *J. Mater. Sci.* **16** (1981) 809.
29. G. E. LLOYD, *Mineral. Mag.* **51** (1987) 3.
30. J. G. SKEDROS, R. D. BLOEBAUM, K. N. BACHUS and T. M. BOYCE, *J. Biomed. Mater. Res.* **27** (1993) 47.
31. J. G. SKEDROS *et al*., *ibid.* **27** (1993) 57.
32. T. M. BOYCE, R. D. BLOEBAUM, K. N. BACHUS and J. G. SKEDROS, *Scanning Microscopy* **4**(3) (1990) 591.
33. A. BOYDE and S. J. JONES, *Metab. Bone Dis. and Rel. Res.* **5** (1983) 145.
34. A. CARDEN *et al*., *Calcified Tissue Intern.* **72** (2003) 166.
35. C. P. TARNOWSKI, M. A. IGNELZI and M. D. MORRIS, *J. Bone Miner. Res.* **17** (2002) 1118.
36. H. HERTZ, *J. Reine Angew Math* **92** (1881) 156.
37. R. G. MUNRO, "Elastic Moduli Data for Polycrystalline Ceramics," in *NISTIR 6853*. National Institute of Standards and Technology, Gaithersburg, Maryland 20899, 2002.
38. S. WEINER and W. TRAUB, *The FASEB Journal* **6** (1992) 879.
39. M. J. GLIMCHER, in "Metabolic Bone Disease," 2nd ed., edited by L.V. Alvioli (Grune and Stratton, Inc., Orlando, Fl, 1987) Chapter 3, p. 49.
40. E. P. KATZ and S. T. LI, *J. Mol. Bio.* **80** (1973) 1.
41. V. B. ROSEN, L. W. HOBBS and M. SPECTOR, *Biomaterials* **23**(3) (2002) 921.
42. A. COURTNEY, W. C. HAYES and L. J. GIBSON, *J. Biomech.* **29** (1996) 1463.
43. S. P. KOTHA and N. GUZELSU, *ibid.* **36** (2003) 1683.
44. R. T. HART, in "Bone Mechanics," edited by S. C. Cowin (CRC Press, Boca Raton, Florida, 1989) p. 54.
45. H. J. QI, K. TAI and C. ORTIZ, (2004) in preparation.
46. Z. FAN and J. Y. RHO, *J. Biomed. Mater. Res. A* **67** (2003) 208.
47. J. Y. RHO *et al*., *J. Biomechanics* **35** (2002) 189.
48. M. E. ROY *et al*., *J. Biomed. Mater. Res.* **44** (1999) 191.
49. D. T. REILLY, A. H. BURSTEIN and V. H. FRANKEL, *J. Biomech.* **7** (1974) 271.
50. Z. FAN *et al*., *J. Orthop. Res.* **20** (2002) 806.
51. J. D. CURREY, *J. Biomech.* **21** (1988) 131.
52. S. N. DANILCHENKO *et al*., *Cryst. Res. Technol.* **39** (2004) 71.
53. K. J. VAN VLIET *et al*., *Phys. Rev. B* **67** (2003) 104105.
54. T. GUTSMANN *et al*., *Biophys. J.* **84** (2003) 2593.
55. S. K. SARKAR *et al*., *Biochemistry* **26** (1987) 6793.
56. S. N. VAIDYA *et al*., *J. Mater. Sci.* **32** (1997) 3213.
57. M. C. BOYCE *et al*., *J. Mech. Phys. Solids* **49** (2001a) 1073.
58. *Idem*., *ibid.* **49** (2001b) 1343.

Received 20 April 2004
and accepted 3 February 2005